Single-cell magnetic imaging using a quantum diamond microscope

David R Glenn[1,8], Kyungheon Lee[2,8], Hongkun Park[3–5], Ralph Weissleder[2,6], Amir Yacoby[3], Mikhail D Lukin[3], Hakho Lee[2], Ronald L Walsworth[1,3,5] & Colin B Connolly[7]

We apply a quantum diamond microscope for detection and imaging of immunomagnetically labeled cells. This instrument uses nitrogen-vacancy (NV) centers in diamond for correlated magnetic and fluorescence imaging. Our device provides single-cell resolution and a field of view (~1 mm^2) two orders of magnitude larger than that of previous NV imaging technologies, enabling practical applications. To illustrate, we quantified cancer biomarkers expressed by rare tumor cells in a large population of healthy cells.

© 2015 Nature America, Inc. All rights reserved.

Overcoming image degradation caused by autofluorescence and light scattering in complex media is a longstanding and important challenge in optical microscopy. Immunofluorescence imaging inevitably suffers from the admixture of the target signal with unwanted autofluorescence intrinsic to the sample, which cannot be completely removed by spectral filtering[1]. Furthermore, optical excitation and fluorescence collection are impeded by scattering and absorption in tissue or complex biofluids[2], leading to reduced resolution in microscopy and degraded sensitivity in rapid detection modalities such as flow cytometry. A promising alternative approach is magnetic imaging of cells immunologically targeted with magnetic nanoparticles (MNPs), which can provide exceptional detection sensitivity owing to the low natural magnetic background in most biological samples[3]. Magnetic measurements of MNP-labeled cells have been realized with several existing technologies, including magnetoresistive sensors[4,5], miniaturized NMR devices[6,7] and Hall-effect sensors[8,9]. To date, however, quantitative magnetic imaging of MNP-labeled biosamples under ambient conditions has not been possible with both single-cell resolution and scalability to macroscopic samples. Here we report a promising solution to this problem using a new optical magnetic imaging modality known as the quantum diamond microscope[10–12], which employs a transparent diamond chip sensor that is biocompatible[13] and easily integrated with standard microscope technology.

The quantum diamond microscope (**Fig. 1a**) employs a dense layer of fluorescent quantum sensors, based on NV color centers, near the surface of a diamond chip on which the sample of interest is placed. The electronic spins of the NV centers are coherently probed with microwaves and are optically initialized and read out to provide spatially resolved maps of local magnetic fields. The magnetic field–dependent NV fluorescence occurs in parallel over the full ensemble of NVs at the diamond surface, resulting in a wide-field magnetic image with adjustable spatial pixel size set by the parameters of the imaging system. In principle, the number of independent magnetic detection channels for such a sensor is limited only by the number of available camera pixels and the sensor size relative to the optical diffraction limit, providing near-arbitrary image pixel size and field of view, with no intervening dead space.

To demonstrate the utility of the quantum diamond microscope for quantitative molecular imaging with single-cell resolution, we configured the instrument for a particular task: rapid detection and magnetic imaging of a small number of cancer cells dispersed in a sample volume containing many background cells. The target cells were labeled with MNPs to indicate the presence of antigens associated with circulating tumor cells[14]. To enable this application, we realized several notable methodological advances over an earlier prototype applied to imaging of magnetotactic bacteria[12]. These included the use of an isotopically enriched diamond substrate, the correction of lowest-order magnetic bias field inhomogeneity, and a substantial suppression of technical noise. These upgrades considerably improved the utility of the quantum diamond microscope, increasing the field of view by two orders of magnitude with no degradation in sensitivity compared to the earlier device.

We first verified the NV-diamond magnetic imaging protocol using model samples prepared by magnetically labeling SKBR3 cancer cells with HER2-specific MNPs (**Fig. 1b**,**c**). MNP-labeled cells were further stained with fluorescent dye (carboxyfluorescein succinimidyl ester, or CFSE) to enable cell identification by *in situ* fluorescence. A solution containing a mixture of labeled and unlabeled cells was placed on the diamond surface, and then a series of correlated bright-field, fluorescence and magnetic images were acquired using a field of view of 1 mm × 0.6 mm. Comparison of bright-field and fluorescence images (**Fig. 2a**) to magnetic images (**Fig. 2b**) verified that all MNP-labeled cells were detected with good signal-to-noise ratio (SNR), whereas all

[1]Harvard-Smithsonian Center for Astrophysics, Cambridge, Massachusetts, USA. [2]Center for Systems Biology, Massachusetts General Hospital, Boston, Massachusetts, USA. [3]Department of Physics, Harvard University, Cambridge, Massachusetts, USA. [4]Department of Chemistry and Chemical Biology, Harvard University, Cambridge, Massachusetts, USA. [5]Center for Brain Science, Harvard University, Cambridge, Massachusetts, USA. [6]Department of Systems Biology, Harvard Medical School, Boston, Massachusetts, USA. [7]Quantum Diamond Technologies, Inc., Somerville, Massachusetts, USA. [8]These authors contributed equally to this work. Correspondence should be addressed to H.L. (hlee@mgh.harvard.edu), R.L.W. (rwalsworth@cfa.harvard.edu) or C.B.C. (cconnolly@quantumdiamondtech.com).

RECEIVED 2 DECEMBER 2014; ACCEPTED 14 MAY 2015; PUBLISHED ONLINE 22 JUNE 2015; DOI:10.1038/NMETH.3449

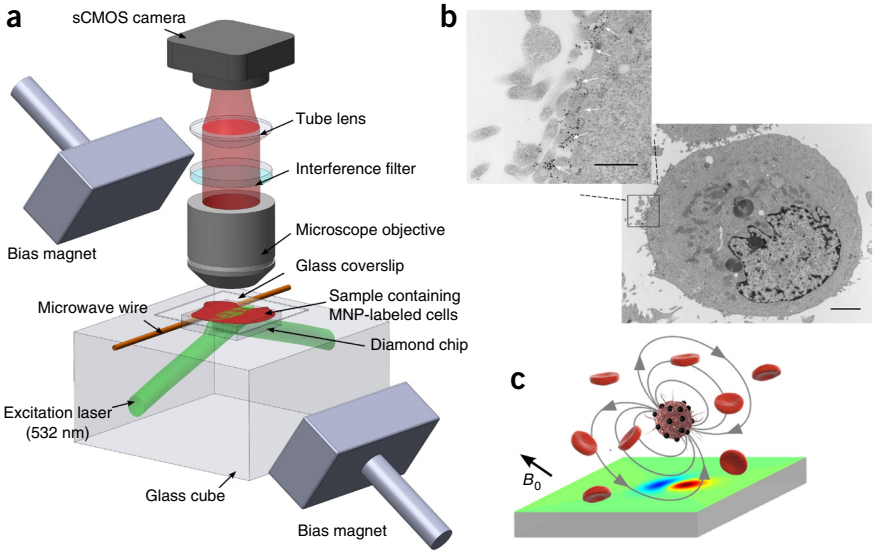


Figure 1 | Quantum diamond microscope for magnetically labeled targets. (**a**) Wide-field NV diamond magnetic imaging microscope. Samples containing immunomagnetically labeled cells are placed directly on the surface of a diamond chip with a highly enriched surface layer of NV centers. NV electronic spins are probed by optically detected magnetic resonance using 532-nm laser light and microwaves, with NV fluorescence imaged onto a scientific complementary metal-oxide semiconductor (sCMOS) camera. For each imaging pixel this procedure determines the magnetic field projection along one of the [111] diamond axes over a 1 mm × 0.6 mm field of view. Diagram adapted from ref. 12, Nature Publishing Group. (**b**) Electron micrograph of a SKBR3 cell labeled with magnetic nanoparticles (MNPs) conjugated to HER2 antibodies. Expanded view: MNPs are visible as black dots on the cell membrane (indicated by white arrows). Scale bars: 2 µm in main figure, 500 nm in inset. (**c**) Diagram of an MNP-labeled target cell above the diamond surface, surrounded by unlabeled normal blood cells. MNP labels are magnetized by the externally applied magnetic bias field B_0, which is aligned as shown with the diamond [111] axis. The magnetic field produced by the MNPs is imaged using the shallow NV layer near the diamond surface to produce the characteristic dipole-like pattern shown (distorted here for perspective).

© 2015 Nature America, Inc. All rights reserved.

unlabeled cells were rejected in less than 1 min of magnetic signal acquisition. For example, in a typical field of view (**Fig. 2a**,**b**), every one of 86 labeled cells (as identified by fluorescence) in a total sample of 436 cells also produced a detectable magnetic field signature. The characteristic two-lobed magnetic field pattern produced by the MNP-labeled cells matched well with models assuming a roughly spherical distribution of magnetic dipoles (**Fig. 1c** and **Supplementary Note 1**). This pattern could be reliably fit to an analytic function to extract the peak magnetic field magnitude, which we refer to here as the magnetic signal. The procedure allowed us to resolve the relative positions of labeled cells even in cases where adjacent cells were touching (**Supplementary Note 2**). For cells displaying relatively strong expression of the labeled antigen (such as the HER2 biomarker on the SKBR3 cell line shown), we observed magnetic signals on the order of 3 µT, compared to a noise floor of ~200 nT under these imaging conditions.

We next performed a titration measurement to assess the fidelity of the quantum diamond microscope for rare-cell detection. Samples of SKBR3 cells were labeled with HER2-specific MNPs and were then mixed in the appropriate volumetric ratios with samples of otherwise identical unlabeled cells to produce mixtures with known labeled fractions. Each mixture was then repeatedly measured in bright-field and magnetic imaging modes, and the fraction of cells producing magnetic field signatures above the detection threshold was tabulated. The rate of magnetic cell detection for each sample corresponded well with the expected fraction of labeled cells based on the mixing ratios (**Fig. 2c**), indicating high detection fidelity.

We further evaluated the quantum diamond microscope's ability to quantify biomarker expression by detecting MNP-labeled cells across a range of cell lines using different target antigens. Samples of cells from three breast cancer lines (SKBR3, MCF7 or MDA-MB-231) were individually incubated with one of three separate MNP preparations, each targeting a different putative cancer biomarker (EGFR, EpCAM or HER2), for a total of nine cell-biomarker combinations. Each sample was magnetically imaged over multiple fields of view, and histograms of the magnetic signals associated with each cell-biomarker combination were accumulated (**Fig. 2d**,**e**). In parallel, cells from the same lines were alternatively labeled with fluorescent antibodies, and marker expression was measured by fluorescence flow cytometry (FC). The distribution widths for magnetic detection were comparable to those in the FC data, indicating that magnetic detection had not introduced extra fluctuations in signal intensity above the natural variability in biomarker expression. Furthermore, comparison of the two measurements showed strong correlation of the mean magnetic signals with mean FC fluorescence intensity (Pearson coefficient $r = 0.985$; **Fig. 2f**), validating the utility of the quantum diamond microscope as a quantitative imaging platform.

The quantum diamond microscope uses NV centers in diamond to obtain co-registered optical and magnetic images of targets labeled with MNPs. The results presented here demonstrate rapid imaging of magnetic fields over an ~1 mm^2 field of view, enabling unambiguous detection of magnetically labeled cells. More generally, this technology provides dynamically reconfigurable (cellular or subcellular) magnetic imaging with resolution down to the optical diffraction limit (**Supplementary Note 3**), over a continuous and transparent sensing surface suitable for integration with multiplexed optical microscopy. The superparamagnetic MNPs used for labeling provide a strong additive magnetic signal, facilitating quantitation of biomarker expression with negligible magnetic background and straightforward sample preparation. Furthermore, the technique is intrinsically robust to complex sample media: the spectrally narrow NV spin resonance used to optically determine the magnetic field is unaffected by other fluorescence sources; green light used for NV excitation is constrained to pass through the side faces of the diamond chip by total internal reflection, thereby protecting the sample from unwanted optical interactions; and the NV fluorescence can be collected through the back face of the diamond without interacting with an optically active or obscuring sample such as

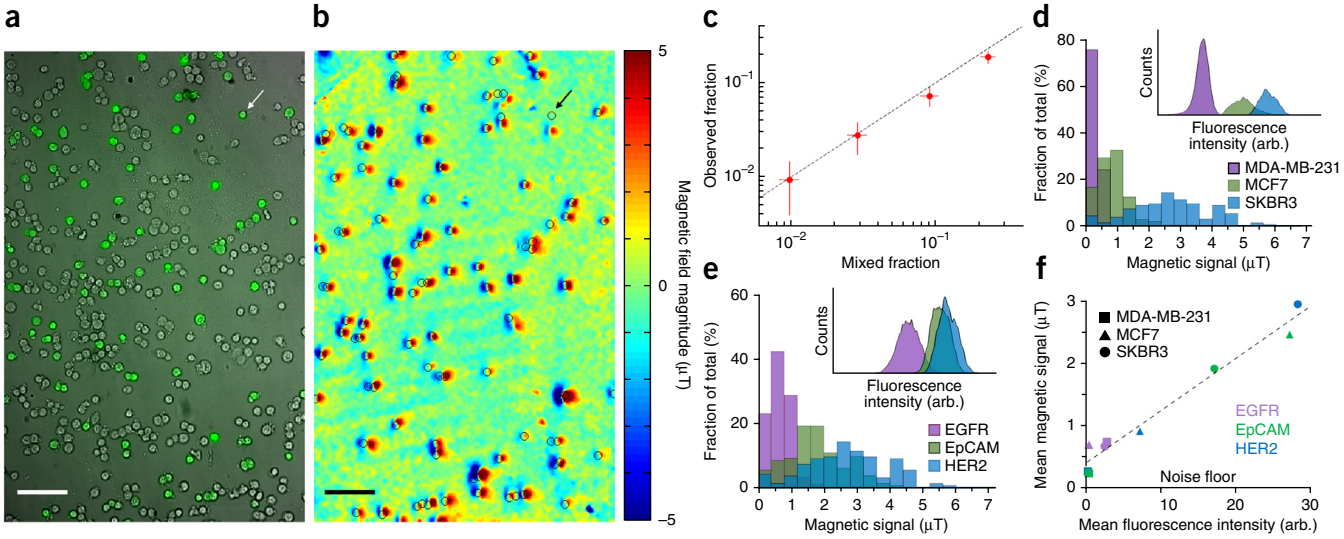


Figure 2 | Wide-field imaging for quantitative magnetic measurement of biomarker expression on multiple cell lines. (**a**) Colocalized bright-field and fluorescence images of a mixture of two subsamples of SKBR3 cells, of which one subsample has been magnetically labeled with magnetic nanoparticles (MNPs) conjugated to HER2 antibodies and stained with fluorescent dye. The fluorescence overlay identifies the MNP-labeled cells. (**b**) Magnetic field image of the same field of view shown in **a**, with all magnetically labeled cells producing characteristic dipole-like patterns. One cell (arrows) moved during acquisition; otherwise the detection rate was 100%. Scale bars, 100 μm. (Images **a** and **b** are representative of three sets of correlated images taken of the same sample under these conditions.) (**c**) Measured fraction of imaged cells producing a magnetic signal >1 μT as a function of the mixed fraction of labeled cells. Correspondence indicates good detection fidelity. Error bars, Poissonian s.d. (N > 200 at each point). (**d**) Histogram of magnetic signals for three cancer cell lines, labeled by MNPs conjugated to anti-HER2. Inset shows flow cytometry (FC) fluorescence intensity distributions (logarithmic horizontal axis; arbitrary units) for different samples of the same cell cultures, labeled by anti-HER2–conjugated fluorophores. (**e**) Histogram of magnetic signals for three samples of SKBR3 cells labeled with MNPs conjugated to antibodies for three different common biomarkers of circulating tumor cells. Inset shows comparison FC data, as in **d**. (**f**) Measured magnetic distribution means vs. FC fluorescence distribution means for all nine cell-biomarker combinations. Linear correspondence (r = 0.985) shows that the magnetic signal reliably quantifies biomarker expression.

blood (**Supplementary Note 4**). The unique combination of features provided by the quantum diamond microscope can now be used to address a range of interesting problems, including those that involve other immunomagnetically labeled targets, such as pathogen detection or the molecular profiling of microvesicles. Other processes can also be associated with magnetic signatures to enable (i) study of the cellular uptake of magnetic nanoparticles with different surface chemistry and (ii) precise measurements of the differential accumulation of nanoparticles among widely varying cell types (for example, cancer cells vs. macrophages). Finally, the quantum diamond microscope may enable imaging of magnetically labeled targets in opaque tissue samples, with transverse spatial resolution approximately equal to the distance between the target and the diamond sensor.

METHODS

Methods and any associated references are available in the online version of the paper.

Note: Any Supplementary Information and Source Data files are available in the online version of the paper.

ACKNOWLEDGMENTS

The authors thank M.L. McKee for help with electron microscopy, as well as M. Liong and H. Shao for advice on magnetic assay protocols. This work was supported in part by US National Institutes of Health grants R01HL113156 (H.L.) and U54-CA119349 (R.W.) as well as the US Defense Advanced Research Projects Agency (DARPA) QuASAR program and DARPA SBIR contract W31P4Q-13-C-0064.

AUTHOR CONTRIBUTIONS

D.R.G. and R.L.W. designed and constructed the quantum diamond microscope. C.B.C., H.L. and R.L.W. conceived the application of the quantum diamond microscope to the task of rare-cell detection and devised the experiments. K.L., R.W. and H.L. developed the optimal protocol for magnetic labeling of cells. K.L. prepared magnetic nanoagents and carried out the cell labeling. D.R.G. and C.B.C. performed the experiments and analyzed the data. C.B.C., D.R.G., K.L., H.L. and R.L.W. wrote the manuscript, with discussion and input from all authors. A.Y., H.P., M.D.L. and R.L.W. conceived the application of NV diamond wide-field magnetic imaging to biomagnetism.

COMPETING FINANCIAL INTERESTS

The authors declare competing financial interests: details are available in the online version of the paper.

Reprints and permissions information is available online at http://www.nature.com/reprints/index.html.

1. Billinton, N. & Knight, A.W. *Anal. Biochem.* **291**, 175–197 (2001).
2. Visser, T.D., Groen, F.C.A. & Brakenhoff, G.J. *J. Microsc.* **163**, 189–200 (1991).
3. Issadore, D. *et al. Lab Chip* **14**, 2385–2397 (2014).
4. Osterfeld, S.J. *et al. Proc. Natl. Acad. Sci. USA* **105**, 20637–20640 (2008).
5. Gaster, R.S. *et al. Nat. Med.* **15**, 1327–1332 (2009).
6. Lee, H., Sun, E., Ham, D. & Weissleder, R. *Nat. Med.* **14**, 869–874 (2008).
7. Lee, H., Yoon, T.-J., Figueiredo, J.-L., Swirski, F.K. & Weissleder, R. *Proc. Natl. Acad. Sci. USA* **106**, 12459–12464 (2009).
8. Issadore, D. *et al. Sci. Transl. Med.* **4**, 141ra92 (2012).
9. Gambini, S., Skucha, K., Liu, P.P., Kim, J. & Krigel, R. *IEEE J. Solid-State Circuits* **48**, 302–317 (2013).
10. Taylor, J.M. *et al. Nat. Phys.* **4**, 810–816 (2008).
11. Pham, L.M. *et al. New J. Phys.* **13**, 045021 (2011).
12. Le Sage, D. *et al. Nature* **496**, 486–489 (2013).
13. Tang, L., Tsai, C., Gerberich, W.W., Kruckeberg, L. & Kania, D.R. *Biomaterials* **16**, 483–488 (1995).
14. Yu, M., Stott, S., Toner, M., Maheswaran, S. & Haber, D.A. *J. Cell Biol.* **192**, 373–382 (2011).

© 2015 Nature America, Inc. All rights reserved.

ONLINE METHODS

Magnetic imaging by optically detected magnetic resonance (ODMR). The negatively charged NV color center is a stable point defect in diamond, consisting of a substitutional nitrogen adjacent to a vacancy in the lattice. In the $S = 1$ electronic ground state, the $m_s = 0$ and $m_s = \pm 1$ spin projection sublevels are split by approximately 2.87 GHz at zero magnetic field. Spin state–dependent decay from the excited triplet electronic state to metastable singlet states allows optical polarization into the $m_s = 0$ state, as well as fluorescent readout of the NV spin state[15]. The projection of the local magnetic field, B, along the NV axis is determined by measuring the Zeeman-induced splitting of these sublevels ($\Delta = \gamma B$, for NV gyromagnetic ratio $\gamma = 2.8$ MHz/gauss) using coherent microwave manipulation. A straightforward implementation of static-field magnetometry with NV centers, employed in the present work, uses optically detected magnetic resonance (ODMR), in which green light at 532 nm continuously drives the NV electronic transition while a continuous-wave microwave source is scanned near one of the $m_s = 0 \rightarrow m_s = \pm 1$ ground-state spin transitions, and the resulting Stokes-shifted fluorescence from the NV center or NV ensemble is monitored. When the microwave drive comes into resonance with the Zeeman-shifted NV spin transition, the steady-state NV population in the $m_s = 0$ ground state is reduced, resulting in a detectable decrease in fluorescence due to temporary NV shelving in the metastable singlet state. The magnetic field sensitivity is determined by the precision of the ODMR frequency measurement, given roughly by the resonance line width divided by the fluorescence SNR. With a bias magnetic field ($B_0 \approx 400$ gauss) aligned along one of the four possible NV axes (i.e., a [111] axis in the diamond lattice), the ensemble of NV centers aligned with that 'sensor' axis is spectrally distinguishable from the other three (degenerate) NV orientation classes. At the diamond chip's magnetic imaging surface, spatial variations of the magnetic field projection along the sensor direction induce local Zeeman shifts in NV spin transition frequencies[11]. ODMR is performed simultaneously on the $m_s = 0 \rightarrow m_s = +1$ and $m_s = 0 \rightarrow m_s = -1$ transitions to correct for possible systematic effects due to internal strain in the diamond[15].

NV-diamond magnetic imaging system. Magnetic field images were acquired by spectroscopic interrogation of NV centers near the surface of a synthetic monocrystalline diamond chip (2 mm × 2 mm × 0.5 mm). The diamond was grown using chemical vapor deposition (CVD) by Element Six, Ltd., with high-purity precursor gases to limit ^{13}C concentration to 10^{-5}. (This concentration, well below the natural abundance of ~1.1%, significantly reduces the effect of interactions with spin-1/2 ^{13}C nuclei in the vicinity of the NV centers.) The diamond was implanted with $^{14}N^+$ ions at 14-keV beam energy, resulting in a highly enriched layer of nitrogen ~10 nm thick at a mean depth of ~20 nm below the surface (estimated using Stopping and Range of Ions in Matter (SRIM) software). Vacuum annealing was carried out to efficiently convert implanted ^{14}N and vacancies into NV centers in the following sequence: ramp from room temperature to 400 °C over 2 h, then hold for 2 h; ramp from 400 °C to 800 °C over 2 h, then hold for 8 h; ramp from 800 °C to 1,100 °C over 2 h, then hold for 3 h. The estimated final NV density in the surface layer was $3 \times 10^{11}/cm^2$, and the measured ODMR line width of each NV hyperfine transition was approximately 600 kHz FWHM. We note that a number of technical improvements related to diamond chip fabrication, microwave delivery and MNP labeling procedures will significantly increase the sensitivity and utility of a next-generation device (**Supplementary Note 5**).

Samples to be imaged (fixed, MNP-labeled cells in buffer solution or blood, as described below) were applied directly to the diamond surface with the shallow NV layer. Imaging was sufficiently rapid that cellular adhesion to the diamond was not required. (Note that it has been shown previously[12] that NV magnetic imaging performance is not significantly impeded by the addition of a layer of poly(L-lysine) on the diamond surface to immobilize cells when necessary. More complex cell-attachment strategies should also be workable, as long as the adhesion layer thickness does not exceed the desired spatial resolution.) Light from a diode-pumped solid-state laser (Coherent Verdi) at 532 nm was directed into the bottom of the diamond chip through a glass cube, to which the diamond was affixed with a thin layer of optical adhesive (Norland NBA107). The angle of incidence was chosen to be below the critical angle for total internal reflection within the diamond at the surface with the NV layer, so that none of the laser light could propagate out from the diamond surface and through the sample. The laser spot size could be varied up to a maximum of approximately 1 mm × 0.6 mm, with an estimated average intensity of approximately 30 W/cm^2. NV fluorescence was collected using a home-built microscope consisting of an objective (Zeiss Plan Apochromat, 20×/0.8), an interference filter (Semrock LP02-633RU), a tube lens (ThorlabsAC254-100-B-ML) and an sCMOS camera (Andor Neo). The tube lens had focal length $f = 10$ cm, chosen to halve the standard magnification of the objective (approximately), at the expense of slight image distortion near the edges of the field of view. Camera exposures were 25 ms in duration for each microwave frequency step. The microwave ODMR signal was provided by a low-noise synthesizer (Agilent E4428C) with sweeps over the $m_s = 0 \rightarrow m_s = -1$ (frequency $f_0 \approx 1.64$ GHz) and $m_s = 0 \rightarrow m_s = +1$ ($f_0 \approx 4.09$ GHz) resonances interleaved point by point. A switch (Mini-Circuits ZASWA-2-50DR) was used to alternate between two amplifiers (Mini-Circuits ZHL-10W-2G and ZHL-16W-43-S) in the appropriate frequency bands for each resonance, and the output microwave signal was applied to the diamond and NV spins through a pair of small (~200-μm diameter), closely spaced wires. The entire experiment was controlled using home-built Matlab software, with a programmable TTL pulse generator (Spincore Pulseblaster) used to synchronize switches and other hardware.

Magnetic image analysis. Analysis of ODMR fluorescence data for characterization of NV-based MNP-labeled cell detection was carried out in two parts: (i) fitting of raw ODMR data to extract pixelwise magnetic resonance line shapes, from which local magnetic field strengths could be determined, and (ii) processing of wide-field magnetic images and correlated bright-field and/or fluorescence images to determine the positions and intensities of magnetic signals from labeled cells. Pixel-by-pixel fitting was performed on the ODMR fluorescence images acquired directly from the camera, sometimes with additional binning to average spectra in adjacent pixels for improved SNR. (For the image shown in **Fig. 2b**, binning was 3 × 3 in hardware and 2 × 2 in software, resulting in a total binned image pixel size of 3.5 μm.)

© 2015 Nature America, Inc. All rights reserved.

In each binned pixel, a sum of three Lorentzian line shapes was fit to the fluorescence intensity as a function of microwave frequency, with the frequency splitting between the peaks fixed to the known ^{14}N longitudinal hyperfine splitting of 2.2 MHz in NV centers[16]. This fit was carried out independently for the $m_s = 0 \rightarrow m_s = -1$ and $m_s = 0 \rightarrow m_s = +1$ transitions. Each NV hyperfine triplet was fit with a single variable line-width parameter and three variable amplitudes to account for variations over the field of view in microwave drive power and ^{14}N nuclear polarization[17], respectively. A single frequency parameter was fit to the central resonance frequency of each hyperfine triplet, and the difference in frequencies for the two transitions was calculated to determine the local magnetic field projection in the pixel: $B = (f_{0\rightarrow+1} - f_{0\rightarrow-1})/2\gamma$, for the NV gyromagnetic ratio γ = 2.8 MHz/gauss. Finally, a quadratic background subtraction was performed over the full magnetic image to remove the effect of bias field inhomogeneity (typically about 10^{-3} of the mean bias field value over a ~1 mm^2 field of view). The processed magnetic image was displayed using the default 64-color 'jet' color map lookup table in Matlab.

The full magnetic image was then compared to spatially correlated bright-field and/or fluorescence images to characterize the magnetic labeling of the sample cells. Cell locations were determined using an automated circle-finding algorithm (circular Hough), and the image was segmented into regions containing clusters of contiguous cells. A two-dimensional fit function was constructed from the cell locations, consisting of one approximate 'dipole' pattern for each cell in the cluster. Dipoles were modeled by the product of a Gaussian function in the vertical direction and the first derivative of a Gaussian in the horizontal direction; the spatial centers of each such dipole were fixed relative to each other to correspond to the relative cell positions, but the overall center of the pattern was allowed to vary. Widths of the Gaussian and Gaussian derivative functions were also fixed, and the amplitude of each dipole was left as a free parameter. The list of least-squares fit dipole amplitudes for each cell-cluster subimage was recorded, and histograms of dipole intensities accumulated as shown (**Fig. 2d–f**) in the main text. (A total of 126 fields of view were imaged to generate the data displayed in these histograms. The numbers of cells measured in each sample were as follows: 171 SKBR3/HER2; 170 SKBR3/EpCAM; 194 SKBR3/EGFR; 125 MCF7/HER2; 107 MCF7/EpCAM; 274 MCF7/EGFR; 156 MDA-MB-231/HER2; 117 MDA-MB-231/EpCAM; 99 MDA-MB-231/EGFR.) We determined an imaging noise floor of approximately 200 nT by applying our image processing and signal-fitting procedures to a set of 1,000 images of randomly generated noise. This noise was chosen to have the same magnitude and spatial scale as that measured in images with no cell sample present. The full data analysis software is available from corresponding author R.L.W. upon request.

Cell lines. The following cell lines were purchased from the American Type Culture Collection (ATCC): SKBR3, MCF7 and MDA-MB-231. All cell lines were tested for mycoplasma- and authenticated by the vendor. The cells were cultured in Dulbecco's modified Eagle's medium (Cellgro) or RPMI 1640 (Cellgro) medium supplemented with fetal bovine serum (FBS, Cellgro, 10%), penicillin and streptomycin (Cellgro, 1%), and L-glutamine (1%). Cell lines were cultured at 37 °C in a humidified atmosphere containing 5% CO_2. At 70% confluence, cells were washed with phosphate buffered saline (PBS), trypsinized, and resuspended in PBS solution containing 2% FBS and 1% BSA (C-PBS). Approximately 1.5×10^5 cells were prepared for each experiment and incubated in C-PBS containing antibodies functionalized with magnetic nanoparticles (100 μg Fe per ml).

Antibody preparation. Cells were magnetically labeled through biotin-streptavidin chemistry, targeting three different antigens: human epidermal growth factor receptor 2 (HER2)/neu, epidermal growth factor receptor (EGFR) and epithelial cell adhesion molecule (EpCAM). The following monoclonal antibodies were biotinylated for conjugation with streptavidin-coated MNPs: anti-HER2/neu (trastuzumab, Genentech), anti-EGFR (cetuximab, ImClone Systems) and anti-EpCAM (MAB9601, R&D Systems). Antibodies were purified by Zeba column (Thermo Scientific) and subsequently incubated with sulfosuccinimidyl-6-[biotin-amido]hexanoate (Sulfo-NHS-LC-Biotin solution, Thermo Scientific) overnight at 4 °C. Biotinylated antibodies were then purified by Zeba column to remove excess reagents. Antibody concentrations were determined by absorbance measurements.

Cell labeling. Cells in suspension were incubated with biotinylated antibodies for 20 min at room temperature. Excess antibodies were removed via centrifugation (300*g*, 2 min). Streptavidin-coated superparamagnetic MNPs (Ocean Nanotech, 20-nm magnetite core) in C-PBS were then introduced, and the mixture was incubated for 20 min at room temperature. Excess MNPs were removed by centrifugation, and the MNP-labeled cells were further fixed using a fixation kit (Phosflow, BD Scientific). For the separate fluorescent identification, the MNP-labeled cells were further stained CFSE (CellTrace CFSE Cell Proliferation Kit, Molecular Probes) according to the vendor-recommended protocol.

Flow cytometry measurement. Flow cytometry was used for validation of biomarker expression levels in each cell line. Antibodies were preconjugated with fluorophore (FITC) before cell labeling. Target cells were incubated with antibodies in C-PBS for 20 min at room temperature. The flow cytometry fluorescence measurements were performed using a LSR II flow cytometer (Becton Dickinson), and mean fluorescence intensity was determined using FlowJo software.

15. Doherty, M.W. *et al. Phys. Rep.* **528**, 1–45 (2013).
16. Felton, S. *et al. Phys. Rev. B Condens. Matter Mater. Phys.* **79**, 075203 (2009).
17. Fischer, R., Jarmola, A., Kehayias, P. & Budker, D. *Phys. Rev. B Condens. Matter Mater. Phys.* **87**, 125207 (2013).

© 2015 Nature America, Inc. All rights reserved.

doi:10.1038/nmeth.3449